Multi-pinhole SPECT Calibration: Influence of Data Noise and Systematic Orbit Deviations

Lin Zhou, Kathleen Vunckx and Johan Nuyts

***Abstract*—The geometry of a single pinhole SPECT system with circular orbit can be uniquely determined from a measurement of three point sources, provided that at least two inter-point distances are known. In contrast, it has been shown mathematically that, for a multi-pinhole SPECT system with circular orbit, only two point sources are needed, and the knowledge of the distance between them is not required. In this paper, we report that this conclusion only holds if the motion of the camera is perfectly circular. In reality, the detector heads systematically slightly deviate from the circular orbit, which may introduce non-negligible bias in the estimated parameters and degrade the reconstructed image. An analytical linear model was extended to estimate the influence of both data noise and systematic deviations on the accuracy of the calibration and on the image quality of the reconstruction. It turns out that applying the knowledge of the distances greatly reduces the reconstruction error, especially in the presence of systematic deviations. In addition, we propose that instead of using the information about the distances between the point sources, it is more straightforward to use the knowledge about the distances between the pinhole apertures during multi-pinhole calibration. The two distance-fixing approaches yield similar reconstruction accuracy. Our theoretical results are supported by reconstruction images of a Jaszczak-type phantom scan.**

I. INTRODUCTION

For accurate image reconstruction, a good estimate of the system matrix is required. Determining the system matrix is particularly challenging for small animal imaging with multi-pinhole SPECT using a rotating gamma camera. For (multi-) pinhole SPECT, it is convenient to factorize the system matrix into several contributions. These include

1) the geometry of the idealized pinhole system, where idealized means that the acquisition is modeled as perfect line integrals,
2) the blurring caused by the intrinsic detector resolution and the finite (effective) diameter of the pinholes,
3) the position dependent detector sensitivity, caused by the finite aperture angle of the pinholes and the position dependence of the relevant solid angles.

This paper only studies the estimation of the first contribution to the system matrix. Estimating the related geometrical parameters is called “geometrical calibration” or simply “calibration” in the rest of this paper. Once the position of these idealized projection lines is known, the acquisition model can be further improved by modeling the finite resolution (e.g. by replacing the single line with a tube or a set of lines [1]), and by taking into account the calculated or measured detector sensitivities for each pinhole aperture [2].

For a conventional single pinhole SPECT system with circular camera motion, the (idealized) geometry can be uniquely characterized by seven parameters [3]. It has been proven mathematically and experimentally that a measurement of 3 point sources, of which at least two inter-point distances are known, is necessary and sufficient to determine these geometrical parameters [3].

Compared with single pinhole SPECT, multi-pinhole SPECT systems attract more attention due to the increase of the detection sensitivity, which results in a higher signal-to-noise ratio in the reconstruction image [4]–[9]. As proven mathematically in [10], [11], a rotating multi-pinhole SPECT only requires 2 point sources without any knowledge about their distance with respect to each other. However, our preliminary tests with measured data indicated that if the distance between the point sources is not fixed to its true value, the calibration of the multi-pinhole system can be unstable and the reconstruction may suffer from a large scaling effect (with the reconstructed distances typically smaller than the true ones).

With the mathematical models proposed in [10], [11], a basic assumption is that the acquisition orbit is perfectly circular. In reality, there are always slight deviations between the circular orbit and the actual orbit due to gravity, mechanical imprecisions, or other reasons [12], [13]. Some of the deviations follow a certain pattern (for example a sine-curve) as a function of acquisition angle, and some are more erratic. We call all these *systematic deviations* in the context of this paper. The systematic deviations will introduce bias on the calibration results if we use a calibration method which assumes perfect camera motion. Since the deviations are expected to be very small, the bias was assumed to be negligible in the previous studies.

The calibration procedure we currently use is described in [14]. The calibration phantom is a rigid plexi plate containing three radioactive point sources. It is positioned in the center of the field of view, and a scan is acquired with the same geometry and protocol as those of the animal scan. From this scan, the geometry is estimated using a two-step procedure based on least squares fitting. For all the geometrical parameters and the point sources locations, we give initial values and calculate the coordinates of the point projections. These parameters and locations are then fitted by comparing the estimated projections to the mass centers of the measured point projections using a least squares fitting procedure. Prior knowledge of the distances between the point sources is typically applied during the fit in order to improve the calibration

The authors are with the Dept. of Nuclear Medicine, K.U.Leuven, B-3000 Leuven, Belgium.

This work is supported by F.W.O. grant G.0569.08, by IUAP grant - NIMI and by IMIR project of K.U.Leuven.

stability [15]. In the first step of the procedure, the so-called *conventional calibration*, a single value is fitted for each parameter. This problem is over-determined and has a unique solution. The results are used as the input values of the second step, which we refer to as *refined calibration* [13]. During refined calibration, the detector and the pinhole collimator are considered as one rigid object subject to small translations and rotations. These deviations describing a rigid motion are determined individually for each projection angle. Here, the number of unknowns is very large and the sum of squared differences has probably many local minima. For that reason, a penalty which discourages large translations and rotations is introduced since all the deviations are expected to be small.

The conventional calibration basically estimates the mean value of each parameter. If the systematic deviations lead to non-negligible bias on these mean values, that bias is not corrected for in the second step, because the refined calibration tends to produce perturbative angle dependent adjustments with (nearly) zero mean. In this paper, we show that this bias can degrade the reconstruction image quality, and we propose a method to predict the degradation, which can be used to design robust calibration configurations.

The main goal of this paper is to develop an efficient and reliable approach to predict the degradation in the reconstruction image quality, which is caused by either data noise or systematic deviations. To do this, we extend an analytical linear approximation model, which was previously used to estimate the noise propagation property in single pinhole calibration [15], to investigate the influence of both data noise and systematic orbit deviations on multi-pinhole SPECT calibration. This method first estimates the bias and variance on the estimated parameters (calibration accuracy), and uses these to compute the resolution loss and image deformation in the reconstructed images (reconstruction accuracy). With this method, the stability and accuracy of the calibration/reconstruction results with and without the prior knowledge of the distance are explored. The comprehensive calibration/reconstruction results of a typical point source setup are analyzed both theoretically and with reconstructions of measured data.

The proposed analytical method is fully validated by repeated simulations, therefore it can be considered as a powerful tool to design or optimize the calibration configuration in the future without referring to a large number of time-consuming numerical simulations.

II. OUTLINE OF THE METHOD

For better understanding of the following sections, we first introduce the most relevant notations and symbols used in the remainder of the text. In addition, we classify the calibration problems into several cases, which will be discussed explicitly in section III.

We define the parameter set P_T as the true geometric parameters consisting of both the camera-specific parameters and the locations of the point sources. We use U_0 to denote the original projection of the point sources without the disturbance of noise or systematic deviations, and the symbol U to represent the projection data which are subject to either random noise or systematic deviations, or both. The difference between this "actual" projection and the original projection is thus $\Delta U = U - U_0$. Applying a calibration procedure to U results in the estimated parameter set P. The difference between the estimated and the true parameters is $\Delta P = P - P_T$.

Ideally, the camera follows a perfectly circular motion. Then P_T are constant for all projection angles, and will be denoted as P_0. However, if the camera unexpectedly deviates from the circular orbit, these parameters need to be adjusted as a function of the projection angle. We symbolize this adjustment by $\Delta P_0(k_\theta)$, with k_θ the index of the projection angle. Since $\Delta P_0(k_\theta)$ is not involved in the projection model of conventional calibration, we consider it as a source of error disturbing the projection. To distinguish between the influences of the two error sources, we use ΔU_N and ΔU_D to denote ΔU caused by data noise and systematic orbit deviations, respectively, with ΔU_D a function of $\Delta P_0(k_\theta)$.

Assuming that the effects of the two error sources are independent from each other, we discuss the calibration problems in the following cases:

- Case 0: The projection is ideal ($U = U_0$), thus the geometric parameters are perfectly estimated ($P = P_0$).
- Case 1: The projection U is disturbed by measurement noise ($U = U_0 + \Delta U_N$) and the parameter estimation is done with conventional calibration. The noise on the data introduces uncertainty on each estimated parameter, and this uncertainty will be expressed as variance (or standard deviation, denoted as ΔP_N) on the final parameter estimates ($P = P_0(\pm \Delta P_N)$).
- Case 2: The projection U is subject to systematic orbit deviations ($U = U_0 + \Delta U_D$), and the parameter estimation is done with conventional calibration. The orbit deviations will introduce bias (ΔP_B)[1] on the estimated parameters ($P = P_0 + \Delta P_B$).
- Case 3: The projection is the same as in case 2, but the refined calibration is performed after the conventional calibration to estimate the systematic deviations (denoted as $\Delta P_D(k_\theta)$[2]). The parameters with this refined adjustment are $P(k_\theta) = P_0 + \Delta P_B + \Delta P_D(k_\theta)$.

A summary of all these cases can be found in table I.

Real measurements will be subject to both noise and systematic deviations. However, it is assumed that they are independent such that the contributions can be studied separately. Therefore, we only compute the degradation of image quality in the reconstruction due to ΔP in case 1, 2, and 3 using the analytical method, and then compare the results for a general evaluation about the influence of different error sources and of the application of different calibration procedures.

This paper is organized as follows. In section III-A, the principle of calibration using point sources is briefly explained. The expressions for the projection coordinates U are given as a function of the parameter set P with and without the modeling of systematic deviations. In addition, the use of

---

[1] It is assumed that the systematic deviation $\Delta P_0(k_\theta)$ has (nearly) zero mean, therefore we define ΔP_B as the bias with respect to P_0 rather than $P_0 + \Delta P_0(k_\theta)$.

[2] Note that both $\Delta P_0(k_\theta)$ and $\Delta P_D(k_\theta)$ represent systematic deviations, but the former is the ground truth and the latter is the estimation.

TABLE I

OVERVIEW OF CALIBRATION PROBLEMS

Case	Error Source	True parameter P_T	Projection Data U	Calibration Procedure	Estimated Parameters P
0	-	P_0	U_0	conventional	P_0
1	noise	P_0	$U_0 + \Delta U_N$	conventional	$P_0(\pm\Delta P_N)$
2	systematic deviations	$P_0 + \Delta P_0(k_\theta)$	$U_0 + \Delta U_D$	conventional	$P_0 + \Delta P_B$
3	systematic deviations	$P_0 + \Delta P_0(k_\theta)$	$U_0 + \Delta U_D$	conventional + refined	$P_0 + \Delta P_B + \Delta P_D(k_\theta)$

prior knowledge of distances during the calibration is also described. In section III-B we explain how to apply a linear approximation model to estimate the accuracy on the estimated parameters, such as the standard deviation ΔP_N and the bias ΔP_B obtained with conventional calibration. In section III-C, the measures for the reconstruction accuracy are proposed as a function of projection coordinates and ΔP, and an efficient approach for computing these measures is described for the above mentioned case 1, 2 and 3, respectively. In section III-D, we explain how to verify the proposed analytical method using repeated numerical simulations for each individual case. The truncation modeling is described in section III-E. Details about the analytical study and phantom reconstruction study are given in Section IV. Results are presented in Section V and discussed in Section VI.

III. METHODS

A. Principle of Calibration

1) Point Projection with Perfect Circular Orbit: Following the notations in [3], we describe a multi-pinhole SPECT system with circular camera motion using the following parameters: detector distance d_D[3], focal distances $f_1, f_2, \ldots, f_I$, mechanical offsets $m_1, m_2, \ldots, m_I$ and $n_1, n_2, \ldots, n_I$, electrical offsets e_u and e_v, tilt angle Φ, and twist angle Ψ, with I the total number of pinhole apertures. These parameters are briefly described in Table II and illustrated in Fig. 1. The projection data is acquired at different rotation angles Θ, indexed by k_θ (k_θ = 1, ... ,N_θ, with N_θ the total number of angles). It is assumed that all the parameters are independent of the acquisition angle and remain constant during the acquisition.

Similar to the single pinhole geometry [3], the projection coordinates are expressed as $U = [\ldots, u_{ij}(k_\theta), v_{ij}(k_\theta), \ldots]^T$, where ^{T} denotes the transpose, and the projection coordinates u, v of the calibration point source j (x_j, y_j, z_j) through pinhole aperture i along the k_θ-th projection angle can be written as:

$$u_{ij}(k_\theta) = f_i \frac{m_i - \tilde{x}_j}{d_D - f_i + \tilde{y}_j} + m_i + e_u \quad (1)$$

$$v_{ij}(k_\theta) = f_i \frac{n_i - \tilde{z}_j}{d_D - f_i + \tilde{y}_j} + n_i + e_v \quad (2)$$

in which

$$\begin{bmatrix} \tilde{x}_j \\ \tilde{y}_j \\ \tilde{z}_j \end{bmatrix} = R_3(\Psi) R_2(\Phi) R_1(\theta) \begin{bmatrix} x_j \\ y_j \\ z_j \end{bmatrix} \quad (3)$$

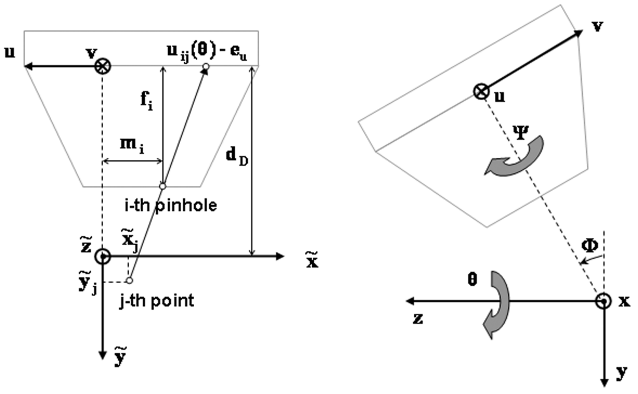

(a) (b)

Fig. 1. (a) Illustration of the geometry parameters along column direction. (b) Illustration of three rotation angles.

with $\theta = \Theta(k_\theta)$ and

$$R_1(\theta) = \begin{bmatrix} \cos\theta & \sin\theta & 0 \\ -\sin\theta & \cos\theta & 0 \\ 0 & 0 & 1 \end{bmatrix} \quad (4)$$

$$R_2(\Phi) = \begin{bmatrix} 1 & 0 & 0 \\ 0 & \cos\Phi & -\sin\Phi \\ 0 & \sin\Phi & \cos\Phi \end{bmatrix} \quad (5)$$

$$R_3(\Psi) = \begin{bmatrix} \cos\Psi & 0 & -\sin\Psi \\ 0 & 1 & 0 \\ \sin\Psi & 0 & \cos\Psi \end{bmatrix} \quad (6)$$

The parameter set to be estimated (P) consists of both camera-specific parameters (d_D, f_i, m_i, n_i, e_u, e_v, Φ, Ψ) and point source locations (x_j, y_j, z_j). For the conventional calibration, we apply (1) and (2) to calculate the locations of the point source projection using the initial estimates for all parameters. The estimates are updated by minimizing the sum of the squared differences between the calculated projections and the centroids of the measured projections.

2) Point Projection with Systematic Deviations: If the orbit of the camera slightly deviates from the assumed perfect circle, the actual geometric parameters described in Table II will vary from projection angle to projection angle. For each acquisition position, the ensemble of the detector and the pinhole collimator can be considered as a rigid object with 6 degrees of freedom, i.e., 3 translation coordinates and 3 rotation angles, all assumed to be small [13]. As shown in Fig. 1, the v-axis is orthogonal to the u-axis, and the distance d_D is measured along the direction perpendicular to the detector plane uv. Therefore we use δd, δu and δv to denote the 3 translation coordinates and $\delta\Phi$, $\delta\Psi$ and $\delta\Theta$ to denote the 3 rotation angles as a function of the rotation angle.

---

[3] It is different from the symbol d used in [3] which represents the distance between the axis of rotation and the pinhole.

TABLE II

d_D	distance between the image center and the detector plane
f_i	focal length of i-th pinhole aperture
m_i, n_i	mechanical offsets of i-th pinhole aperture in detector column/row direction
e_u, e_v	electrical detector offsets in detector column/row direction
Φ	tilt angle, i.e. angle between the detector plane and the axis of rotation (AOR)
Ψ	twist angle, describes the orientation of the detector pixel grid as a rotation around an axis perpendicular to the detector plane

The parameters are adapted as

$$d_D(k_\theta) = d_D + \delta d(k_\theta) \tag{7}$$

$$m_i(k_\theta) = m_i + \delta u(k_\theta) \tag{8}$$

$$n_i(k_\theta) = n_i + \delta v(k_\theta) \tag{9}$$

$$e_u(k_\theta) = e_u - \delta u(k_\theta) \tag{10}$$

$$e_v(k_\theta) = e_v - \delta v(k_\theta) \tag{11}$$

$$\Phi(k_\theta) = \Phi + \delta\Phi(k_\theta) \tag{12}$$

$$\Psi(k_\theta) = \Psi + \delta\Psi(k_\theta) \tag{13}$$

$$\Theta'(k_\theta) = \Theta(k_\theta) + \delta\Theta(k_\theta) \tag{14}$$

Applying (7)-(14) to (1)-(6), we have the general projection equations:

$$u_{ij}(k_\theta) = f_i \frac{m_i(k_\theta) - \tilde{x}_j(k_\theta)}{d_D(k_\theta) - f_i + \tilde{y}_j(k_\theta)} + m_i(k_\theta) + e_u(k_\theta) \tag{15}$$

$$v_{ij}(k_\theta) = f_i \frac{n_i(k_\theta) - \tilde{z}_j(k_\theta)}{d_D(k_\theta) - f_i + \tilde{y}_j(k_\theta)} + n_i(k_\theta) + e_v(k_\theta) \tag{16}$$

with

$$\begin{bmatrix} \tilde{x}_j(k_\theta) \\ \tilde{y}_j(k_\theta) \\ \tilde{z}_j(k_\theta) \end{bmatrix} = R_3(\Psi(k_\theta)) R_2(\Phi(k_\theta)) R_1(\Theta'(k_\theta)) \begin{bmatrix} x_j \\ y_j \\ z_j \end{bmatrix} \tag{17}$$

For the refined calibration, we used the calibrated values of all parameters yielded by the conventional calibration as inputs of (15) and (16) to estimate $\Delta P_D(k_\theta)$, which consists of the k_θ-th elements of δd, δu, δv, $\delta\Phi$, $\delta\Psi$, $\delta\Theta$, using a penalized least squares fitting method.

3) Distance as Prior Knowledge: As mentioned in Section III-A1, besides the camera-specific parameters, the positions of the point sources are also estimated during the conventional calibration. In order to acquire extra robustness of the calibration result, we always take advantage of the information about the distances between the point sources. For three point sources, it is achieved by transforming the Cartesian coordinates of the point sources $[x_j,\ y_j,\ z_j]$ $(j = 1, 2, 3)$ into three translation coordinates $(t_x,\ t_y,\ t_z)$, three rotation angles $(\rho_1,\ \rho_2,\ \rho_3)$ and three distances $(d_{12},\ d_{13},\ d_{23})$ [15]. For two point sources, beside the three translation coordinates, it only yields two rotation angles $(\rho_1,\ \rho_2)$ and one distance (d_{12}). In our case, the three points are small cavities drilled in a rigid plate (which is our so-called *calibration phantom*), thus the distances between the point sources are fixed. The phantom position is then uniquely described by $t_x, t_y, t_z, \rho_1, \rho_2$ and ρ_3, and we only need to estimate these 6 parameters to determine the point source positions.

Similar to the calibration phantom, the configuration of our multi-pinhole plate is also rigid. In principle we can use the same strategy. For the $i-$th pinhole aperture, we take $[m_i, f_i, n_i]$ as the Cartesian coordinates to denote the pinhole position. The coordinate transformation will end up with 3 translation coordinates (t_m, t_f, t_n), 3 rotation angles (ρ_1, ρ_2, ρ_3) and $3 \times (I - 2)$ independent distances $(d_{12}, d_{13}, d_{23}, \ldots, d_{1i}, d_{2i}, d_{3i})$[4]. If the distances between the pinhole apertures are known, we can apply the same approach, i.e., using the inter-pinhole distances to stabilize the calibration result and only fitting the 6 parameters which indicate the position of the pinhole plate in the image space.

With conventional calibration, the number of unknown parameters P depends on whether or not the prior knowledge of the distances will be used, and if so, which distances (inter-point or inter-pinhole) will be fixed during the calibration. An overview is provided in table III.

B. Calibration Accuracy

It is assumed that the relation between ΔU and the small variations in the estimates ΔP can be approximately described using the following linear equation:

$$\Delta U = M \Delta P \tag{18}$$

where M is a matrix containing the first-order derivatives of the projection coordinates U_0 (see (1) and (2)) to each parameter of P_0. The least squares solution of the linear system (18) yields the variations ΔP induced by small errors in the projection coordinates ΔU:

$$\Delta P = (M^T M)^{-1} M^T \Delta U \tag{19}$$

where ^{T} denotes matrix transpose. Note that ΔP in (19) has a single value for each parameter and therefore corresponds to the conventional calibration procedure. We will use (19) to estimate the variance (or the standard deviation ΔP_N) and the bias (ΔP_B) on the estimated parameter P, due to data noise and systematic deviations, respectively.

1) Case 1: If the projection coordinate U is only disturbed by data noise, the noise is better characterized by its covariance matrix $\mathrm{Cov}(U)$ rather than by a single noise realization ΔU_N. The calibration accuracy can then be expressed by the covariance matrix of the estimated parameters P:

$$\mathrm{Cov}(P) = (M^T M)^{-1} M^T \mathrm{Cov}(U) M (M^T M)^{-1} \tag{20}$$

The variance on the $j-$th parameter ($\mathrm{Var}(P_j)$) is the $j-$th diagonal element of the covariance matrix:

$$\mathrm{Var}(P_j) = (\sigma(P_j))^2 = [\mathrm{Cov}(P)]_{jj} \tag{21}$$

We have $\Delta P_N = [\sigma(P_j)]$ with $\sigma(P_j)$ the standard deviation on the j-th parameter.

---

[4] This only holds for $I \geq 3$. If $I = 2$, it will result in 3 translations, 2 rotations and only 1 distance.

TABLE III

UNKNOWN CALIBRATION PARAMETERS PER CALIBRATION METHOD.

Calibration method	Camera-specific parameters	Point source location parameters
No distances fixed	d_D, $f_{i=1,\dots,I}$, $m_{i=1,\dots,I}$, $n_{i=1,\dots,I}$, e_u, e_v, Φ, Ψ	$x_{j=1,\dots,J}$, $y_{j=1,\dots,J}$, $z_{j=1,\dots,J}$
Inter-point distance(s) fixed	d_D, $f_{i=1,\dots,I}$, $m_{i=1,\dots,I}$, $n_{i=1,\dots,I}$, e_u, e_v, Φ, Ψ	3 translations, 2 or 3 rotations
Inter-pinhole distance(s) fixed	d_D, 3 translations, 2 or 3 rotations, e_u, e_v, Φ, Ψ	$x_{j=1,\dots,J}$, $y_{j=1,\dots,J}$, $z_{j=1,\dots,J}$
All distances fixed	d_D, 3 translations, 2 or 3 rotations, e_u, e_v, Φ, Ψ	3 translations, 2 or 3 rotations

2) Case 2: If the projection U is only subject to systematic deviations, we calculate U using (7)-(17) and compute $\Delta U_D = U - U_0$. The bias on the estimated parameters is computed by (19):

$$\Delta P_B = (M^T M)^{-1} M^T \Delta U_D \tag{22}$$

3) Case 3: The bias ΔP_B on the estimated parameters is calculated in the same way as in case 2. With the analytical linear model, there is no straightforward way to estimate $\Delta P_D(k_\theta)$. However, it is still feasible to approximately estimate the reconstruction accuracy with an alternative approach. That approach will be discussed in detail in section III-C.

C. Reconstruction Accuracy

To evaluate the reconstruction accuracy, we use a similar approach as in [15]. Two figures of merit, i.e., the loss of spatial resolution and the deformation in the reconstruction image, are applied to quantify the degradation of the reconstruction accuracy. To this end, a grid of points which is considered sufficiently covering the field of view of the multi-pinhole system is reconstructed analytically. To distinguish between the projection of the calibrating point sources and the projection of this grid of point sources used for reconstruction evaluation, we add the superscript ^{g} in the latter case, with U_0^g and U^g corresponding to the ideal and actual projection coordinates of the point sources on the grid, respectively.

For a point on the grid $X_q = [x_q, y_q, z_q]^T$, the projection ray ((1) and (2)) that goes through this point and the $i-$th pinhole can be expressed in a general format:

$$a_{uiq}(k_\theta)x_q + b_{uiq}(k_\theta)y_q + c_{uiq}(k_\theta)z_q + d_{uiq}(k_\theta) = 0 \tag{23}$$

$$a_{viq}(k_\theta)x_q + b_{viq}(k_\theta)y_q + c_{viq}(k_\theta)z_q + d_{viq}(k_\theta) = 0 \tag{24}$$

or in matrix format

$$A_{uiq}(k_\theta)X_q + B_{uiq}(k_\theta) = 0 \tag{25}$$

$$A_{viq}(k_\theta)X_q + B_{viq}(k_\theta) = 0 \tag{26}$$

Combining the matrices in (25) and (26) of all projection angles, all pinhole apertures and both directions u and v, we have

$$A_q X_q + B_q = 0 \tag{27}$$

with $A_q = [A^T_{u1q}(1), A^T_{v1q}(1), \dots, A^T_{uIq}(N_\theta), A^T_{vIq}(N_\theta)]^T$ and similar for B_q. The dimensions of A_q and B_q are $N_{AB} \times 3$ and $N_{AB} \times 1$, respectively, with $N_{AB} = 2 \times N_\theta \times I$.

If the system is perfectly calibrated, all the parameters get exact values and $X_q^R = [x_q, y_q, z_q]^T$ is the unique solution of (27). However, with noise or systematic deviations on the data, the calibration cannot be perfect and will introduce small variations ΔP in the estimated parameters. This yields matrices ${A'}_q$ and ${B'}_q$ which are functions of U^g and ΔP. As a result, (27) is typically overdetermined. In this case, we calculated the coordinates of the 'reconstructed' point source X_q^R as the least squares solution of the linear equation (27):

$$X_q^R = -({A'}_q^T {A'}_q)^{-1} {A'}_q^T {B'}_q \tag{28}$$

where the arguments U^g and ΔP are dropped for convenience. Using (28) we can estimate the resolution loss and the image deformation as reconstruction accuracy.

The loss of spatial resolution is estimated based on the distance (denoted by $S_{iq}(k_\theta)$) between the reconstructed point $X_q^R = [x_q^R, y_q^R, z_q^R]^T$ and the corresponding back-projection ray through the i-th pinhole aperture along the k_θ-th projection angle. This point-to-line distance equals the square root of the squared sum of the point-to-plane distances between X_q^R and the two planes defined by (25) and (26):

$$S_{iq}(k_\theta) = \tag{29}$$

$$\sqrt{\left(\frac{A'_{uiq}(k_\theta)X_q^R + B'_{uiq}(k_\theta)}{\|A'_{uiq}(k_\theta)\|}\right)^2 + \left(\frac{A'_{viq}(k_\theta)X_q^R + B'_{viq}(k_\theta)}{\|A'_{viq}(k_\theta)\|}\right)^2}$$

where $\|\cdot\|$ represents the Euclidean norm. At each projection angle, we decompose S_{iq} in three directions as $S_{iq} = [s^x_{iq}, s^y_{iq}, s^z_{iq}]^T$, and take the longest length among all three dimensions, all acquisition angles and all points on the grid with back-projection rays through all pinhole apertures as the measure of the resolution loss.

$$\text{Res. Loss} = \max_i(\max_q(\max_\theta(\max_\epsilon(\|s^\epsilon_{iq}(k_\theta)\|)))) \tag{30}$$

where $\epsilon \in (x, y, z)$ indicates the direction of the measure.

The image deformation is evaluated from the relative difference in distance between any two points on the grid before and after the reconstruction[5]. Let p and q be the index of the two points, the corresponding relative difference T_{pq} is defined as

$$T_{pq} = \frac{\|X_p^R - X_q^R\| - \|X_p - X_q\|}{\|X_p - X_q\|} \times 100\% \tag{31}$$

We define the maximal value of T_{pq} among all points combinations on the grid as the image deformation.

$$\text{Img. Def.} = \max_p(\max_q(\|T_{pq}\|)) \tag{32}$$

Note that $S_{iq}(k_\theta)$ and T_{pq} are two arrays which have $3 \times N_\theta \times N_q \times I$ and $N_q \times (N_q - 1)/2$ number of elements, respectively, with N_q the number of points on the grid.

The matrices A'_q and B'_q which yield X_q^R (and subsequently $S_{iq}(k_\theta)$ and T_{pq}) are calculated differently in the noise study

---

[5] Note that the definition of the image deformation is different from that in [15] in order to facilitate the validation.

and in the study of the systematic deviations. In order to simplify the expressions that follow, we first introduce symbols $F_{uviq}(U^g, \Delta P, k_\theta)$ and $F_{pq}(U^g, \Delta P)$ to denote the set of matrices involved, i.e.,

$$\begin{aligned}F_{uviq}(U^g, \Delta P, k_\theta) \equiv\, & A'_{uiq}(U^g, \Delta P, k_\theta), B'_{uiq}(U^g, \Delta P, k_\theta),\\ & A'_{viq}(U^g, \Delta P, k_\theta), B'_{viq}(U^g, \Delta P, k_\theta)\\ F_{pq}(U^g, \Delta P) \equiv\, & A'_p(U^g, \Delta P), B'_p(U^g, \Delta P),\\ & A'_q(U^g, \Delta P), B'_q(U^g, \Delta P)\end{aligned}$$

Next, we will discuss how to compute the measures for the resolution loss ($S_{iq}(k_\theta)$) and the image deformation (T_{pq}) in case 1, 2 and 3.

1) Case 1: If ΔP is only due to data noise, the matrices A' and B' are computed based on U_0^g and the covariance matrix Cov(P). As explained in [15], Cov(P) can be decomposed as Cov(P) $= \Gamma\Gamma^T$. By a linear transformation $\Delta P_N^k = \Gamma e_k$ with $e_k = [0, \ldots, 0, 1, 0, \ldots, 0]^T$ the $k-$th unit vector, it yields parameter estimate errors ΔP_N^1, ΔP_N^2, ..., ΔP_N^K, with K the total number of unknown camera-specific parameters[6]. Since these ΔP_N^k are uncorrelated noise components, it is valid to assume that these errors have an independent effect on the image reconstruction accuracy. Thus they can be added quadratically (see Appendix):

$$S_{iq}(\theta) = \sqrt{\sum_{k=1}^{K} \|S_{iq}(F_{uviq}(U_0^g, \Delta P_N^k, k_\theta))\|^2} \tag{33}$$

$$T_{pq} = \sqrt{\sum_{k=1}^{K} \|T_{pq}(F_{pq}(U_0^g, \Delta P_N^k))\|^2} \tag{34}$$

2) Case 2: If there are only systematic deviations during the acquisition, the matrices A' and B' are computed using $U^g = U_0^g + \Delta U_D^g$ and the bias ΔP_B is generated by (19):

$$S_{iq}(\theta) = S_{iq}(F_{uviq}(U^g, \Delta P_B, k_\theta)) \tag{35}$$

$$T_{pq} = T_{pq}(F_{pq}(U^g, \Delta P_B)) \tag{36}$$

3) Case 3: Although it is not feasible in this case to calculate the calibration accuracy ($\Delta P_B + \Delta P_D(k_\theta)$) with the linear model, we propose an approach to approximate the reconstruction accuracies. Recall that the true systematic deviations and the estimated deviations are $\Delta P_0(k_\theta)$ and $\Delta P_D(k_\theta)$, respectively. It is assumed that $\Delta P_0(k_\theta)$ can be accurately estimated by refined calibration, i.e., $\Delta P_D(k_\theta) \approx \Delta P_0(k_\theta)$. As a result, the influence of systematic deviations is (almost) compensated in the reconstruction procedure, and we expect the resolution loss and the image deformation in case 3 to be predicted with the following equations:

$$S_{iq}(\theta) = S_{iq}(F_{uviq}(U_0^g, \Delta P_B, k_\theta)) \tag{37}$$

$$T_{pq} = T_{pq}(F_{pq}(U_0^g, \Delta P_B)) \tag{38}$$

Note that, since the effects of the systematic deviations are assumed to be canceled out, they are not included in A' and B'. However, since the bias ΔP_B cannot be corrected for by refined calibration, it will still degrade the reconstruction accuracy, and therefore needs to be incorporated in A' and B' in (37) and (38).

D. Validation with Repeated Simulations

The calibration accuracy and the reconstruction accuracy can be validated by numerical simulations.

1) Case 1: For noise propagation, we first calculate the projection U_0 of the calibrating point sources using (1) and (2), then add Gaussian noise on U_0 and perform conventional calibration. For each calibrated parameter, the variance (or the standard deviation) is derived from multiple noise realizations. The calibration of the n-th noise realization will result in a disturbed parameter set ΔP_N^n. Thus, the error measures can be estimated as

$$\hat{S}_{iq}(\theta) = \sqrt{\frac{1}{N_s}\sum_{n=1}^{N_s} \|S_{iq}(F_{uviq}(U_0^g, \Delta P_N^n, k_\theta))\|^2} \tag{39}$$

$$\hat{T}_{pq} = \sqrt{\frac{1}{N_s}\sum_{n=1}^{N_s} \|T_{pq}(F_{pq}(U_0^g, \Delta P_N^n))\|^2} \tag{40}$$

where N_s is the number of noise realizations.

2) Case 2: To verify the reconstruction accuracy with systematic deviations, we use (15) and (16) to generate the calibrating point source projections with deviations but without noise ($U = U_0 + \Delta U_D$), then perform conventional calibration based on the deviated projections. The bias ΔP_B is estimated during the fitting and is used to analytically reconstruct the grid of point sources from U^g. The measures for the resolution loss and the image deformation are calculated in the same way as in section III-C2 with (35) and (36).

3) Case 3: To quantify the reconstruction accuracy corresponding to the two-step calibration procedure, we perform the refined calibration based on $U = U_0 + \Delta U_D$ using the parameters estimated in case 2 ($P_0 + \Delta P_B$) as initial values for the fitting. The refined calibration yields the estimated systematic deviation $\Delta P_D(k_\theta)$, with which the computation for the accuracy measures becomes

$$\hat{S}_{iq}(\theta) = S_{iq}(F_{uviq}(U^g, \Delta P_B + \Delta P_D, k_\theta)) \tag{41}$$

$$\hat{T}_{pq} = T_{pq}(F_{pq}(U^g, \Delta P_B + \Delta P_D(k_\theta))) \tag{42}$$

E. Truncation Modeling

In Section III-A1 and Section III-A2 we provided the equations which yield projection coordinates for each point source through each aperture for all projection angles. In reality, a point source will not always be detected through every pinhole aperture at every projection angle. With the analytical method, this data truncation is modeled by only preserving the columns or rows in U, M and cov(U) ((19) and (20)) corresponding to those projection points that are located in the field of view (FOV) of the aperture and in the valid detector area. With numerical simulation, the truncated point projections are simply not used for the least squares fitting in the calibration procedure. For each pinhole of our multi-pinhole collimators, we determined the aperture FOV on the

---

[6] The parameters related to the point source location do not influence the reconstruction, therefore they are not considered here.

detector from long planar scans of a small plane source put in front of each hole.

IV. STUDIES

We investigated the influence of data noise and systematic deviations on the reconstruction accuracy with both the proposed analytical method and a real measurement. The studies were based on our self-designed 7-pinhole collimators for a typical acquisition setting with dual-head gamma camera. Each designed multi-pinhole plate consists of a central aperture with 6 surrounding apertures located on a circle with a radius of 20 mm. A detailed description, as well as the technical drawing of this pinhole design, can be found in [16]. The calibration phantom in use was a Bequé phantom [15] which consists of three radioactive point sources with 1 mm diameter (Fig. 2(a)). The data were acquired using both detector heads and with 64 projection angles equally spread over 360°. Detector 1 and detector 2 started at the top and the bottom of the gantry respectively and rotated clockwise during the acquisition.

One of the aims is to investigate the influence of applying the prior knowledge about inter-point and inter-pinhole distances on the calibration/reconstruction accuracy. To this end, four different calibration methods were applied to the same data:

- fitting all parameters, including all distances,
- fixing only the inter-point distance(s),
- fixing only the inter-pinhole distances,
- fixing both the inter-point and inter-pinhole distances.

The resolution loss and the image deformation yielded by all these methods are compared.

The other purpose is to find out whether it is enough to use only 2 point sources to do the calibration with adequate accuracy, even in the presence of systematic deviations. As a preliminary test, we separated the projections of the 3 point sources, and performed the calibration with

- projection data of all 3 point sources,
- projection data of the 1st and the 2nd point source,
- projection data of the 1st and the 3rd point source

which are referred to as *3PS*, *2PS-sub12* and *2PS-sub13* in the remainder of the text, respectively. The calibration results and the reconstruction accuracies of 2PS-sub12 and 2PS-sub13 were compared with those of 3PS for each detector head individually.

A. Analytical Evaluation

For the analytical study, typical values were used for P_0. The detector distance (d_D) and the focal length of the pinhole collimator (f) were chosen to be 206 mm and 176 mm, respectively. The mechanical offsets of the pinhole apertures were the same as the designed values [16]. The electrical shifts (e_u, e_v), tilt angle (Φ) and twist angle (Ψ) were expected to be zero. The calibration phantom was positioned in the center of the field of view, and was parallel to the two detector planes at the beginning of the acquisition. The inter-point distances d_{12}, d_{13} and d_{23} were 26 mm, 19 mm and 26 mm, respectively.

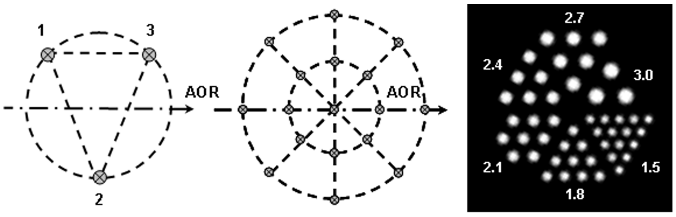

(a) Bequé phantom **(b) Point source grid** **(c) Jaszczak phantom**

Fig. 2. (a) Configuration of the Bequé calibration phantom. (b) Cross section of the grid of points used to evaluate the reconstruction accuracy. The point sources are positioned on two circles with a radius of 10mm/20mm. (c) Transaxial slice of the Jaszczak phantom. The diameters of the hollow rods are given in the unit of millimeter.

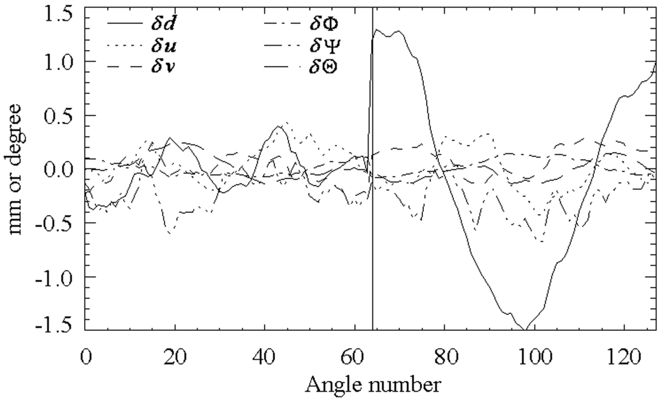

Fig. 3. Plot of the systematic deviation ΔP_0 acquired from a previous refined calibration as a function of angular position k_θ. Different line types represent different degrees of freedom. Angles with number 0-63 and 64-127 are for detector head 1 and head 2, respectively. The translations are expressed in mm, the rotations in degrees.

The analytical linear model described in Section III was applied to evaluate the reconstruction accuracy of different calibration methods combined with different point source settings (3PS, 2PS-sub12 and 2PS-sub13). For the noise propagation study, we modeled the error (ΔU_N) on the determination of the centroid of the projection points due to data noise by a Gaussian distribution with realistic standard deviation of 0.6 mm. For the influence of systematic deviations, we used the deviations estimated from a previous refined calibration procedure with dual-head data as $\Delta P_0(k_\theta)$. All 6 degrees of freedom in $\Delta P_0(k_\theta)$ are plotted in Fig. 3 as a function of k_θ. The two detector heads have very different deviation patterns.

The calibration accuracies, i.e., the variance and the bias on each parameter to be estimated, were calculated by (21) and (22), respectively. The corresponding reconstruction accuracies were calculated as explained in Section III-C. The grid of points that was used to generate U_0^g and U^g had a cross section shown in Fig. 2(b). The radius of the two circles were 10 mm and 20 mm, respectively. The complete grid was obtained by rotating the displayed grid by 0° and 90° around the axis of rotation.

The analytical evaluation was done with both non-truncated and truncated point projections. The results were verified by numerical simulations with 100 noise realizations (see section III-D).

B. Jaszczak Phantom Reconstruction

In order to visually inspect the degradation of the reconstruction quality, we reconstructed a Jaszczak-type phantom using the parameters estimated from different calibration approaches. The Jaszczak-type phantom (Fig. 2(c)) consists of a plastic cylinder with an outer diameter of 40 mm and 6 wedge-shaped sections with multiple hollow rods having a diameter ranging from 1.5 mm to 3.0 mm in steps of 0.3 mm. This configuration facilitates us to closely examine the resolution and the image deformation of the reconstruction image.

We scanned the Jaszczak-type phantom on a clinical dual-head gamma camera (E.cam, Fixed 180°, Siemens Medical Solutions) equipped with the self-designed 7-pinhole collimators. The phantom was filled with 37 MBq ^{99m}Tc and scanned with 30 seconds/view in step-and-shoot mode. The calibration data were acquired immediately after the phantom scan. The three point sources on the calibration phantom were filled with 1.85 MBq ^{99m}Tc each and were scanned using the same geometry but with 10 seconds/view acquisition. The diameter of each point source was 1 mm.

For each calibration approach, the data were reconstructed twice. First, the parameters were estimated based on the conventional calibration procedure which assumes perfect circular camera motion. Second, the parameters adapted by the refined calibration were used. To show the effect of the very different systematic deviation patterns (Fig. 3), the reconstruction was performed for each head separately.

For the reconstruction, the activity distribution of the phantom was reconstructed in a $72 \times 72 \times 88$ image space with 0.6^3 mm^3 voxels. The ordered subset expectation maximization (OSEM) [17] algorithm was used for reconstruction with the following iteration scheme: 5×16, 5×8, 5×4, 5×2, 5×1 (global iteration × number of subsets). Corrections for decay and scatter were applied, attenuation was ignored.

V. RESULTS

A. Analytical Evaluation

As an example of calibration accuracy, the results of detector head 2 with truncation modeling are given in Fig. 4. In the left column the standard deviations ΔP_N on the camera-specific parameters[7] due to noise propagation are plotted. In the right column, the bias on the same parameters (ΔP_B) are shown for the given systematic deviations (Fig. 3). It can be seen that ΔP_N are very small (all less than 0.3 mm or degree), whereas ΔP_B on the same parameters (for example the focus heights f_i) are much more pronounced. The three point settings (3PS, 2PS-sub12 and 2PS-sub13) yield similar noise properties but very different bias on the estimated parameters.

It is not obvious from Fig. 4 which point source setting will result in better reconstruction accuracy. In table IV, table V and table VI we give specific values for resolution loss and image deformation for case 1, 2 and 3, respectively. The figures between the brackets are the corresponding values acquired from numerical simulations presented for validation purpose. The results are shown for both detector heads. Mostly the reconstruction accuracies predicted by our linear approximation model are in good agreement with those obtained from simulations.

There are several points worth noticing in these tables. First, the degradation of the reconstruction quality due to noise is almost the same for the two detector heads, but the degradation due to bias is quite different because of the different systematic deviations. Second, with the given systematic deviations, the reconstruction errors due to noise are negligible compared with those due to bias, even for detector head 1 whose deviations are not pronounced. Third, regardless of the cause of the error, the reconstruction accuracy (especially the image deformation) improved if we applied the prior knowledge of either the inter-point or inter-pinhole distances during the calibration. However the gain hardly increased when we fixed all distances. Fourth, the negative relative deformation values in table V and VI predict that the reconstructed object will be up to 40% smaller than the true object, if no distance information is used during calibration. Fifth, since detector head 2 suffers from more severe systematic deviations than head 1, the corresponding accuracies are much worse. Sixth, with the given point source position, the 2PS-sub12 leads to similar resolution properties as 3PS, whereas 2PS-sub13 results in very bad resolution in the reconstruction. Seventh, comparing table V with table VI, it can be seen that the refined calibration significantly improves the resolution in the reconstruction. However, it hardly affects the scaling effect in the image dimension, especially if no distances were fixed.

Note that all the results presented in this section are calculated based on truncated projections.

B. Jaszczak Phantom Reconstruction

Fig. 5 shows trans-axial slices of 24 reconstruction images (4 calibration methods × 2 calibration procedures (conventional / refined) × 3 point settings) reconstructed using the data of detector head 2. The dimensions of these slices are the same as those of the original one shown in Fig. 2(c).

Before comparing the reconstructions with the analytical predictions, recall that the influence of data noise is negligible compared to that of systematic deviations based on the theoretical analysis. Therefore we expect that table V (case 2) and table VI (case 3) approximately predict the degradation of the image quality in the reconstructions which correspond to the conventional / refined calibration.

From Fig. 5, we can see that if no distance is fixed during the calibration, the reconstruction image is obviously scaled, with scaling factor 2PS-sub12 $>$ 3PS $>$ 2PS-sub13. However, once we fix either inter-point or inter-pinhole distances, the deformation becomes negligible. In all cases, the refined calibration improves the image resolution, but hardly affects the image deformation. The resolution with 2PS-sub12 is comparable with, and sometimes even better than that of 3PS. For instance, the rods with diameter of 2.1 mm are more clear and circular-shaped with 2PS-sub12 rather than with 3PS. The resolution with 2PS-sub13 is however much worse even with refined calibration. These findings are all in accordance with table V and table VI.

---

[7] Because of the large number of camera-specific parameters, we only present the errors on m_i, f_i and n_i for the second, the fourth and sixth pinhole aperture.

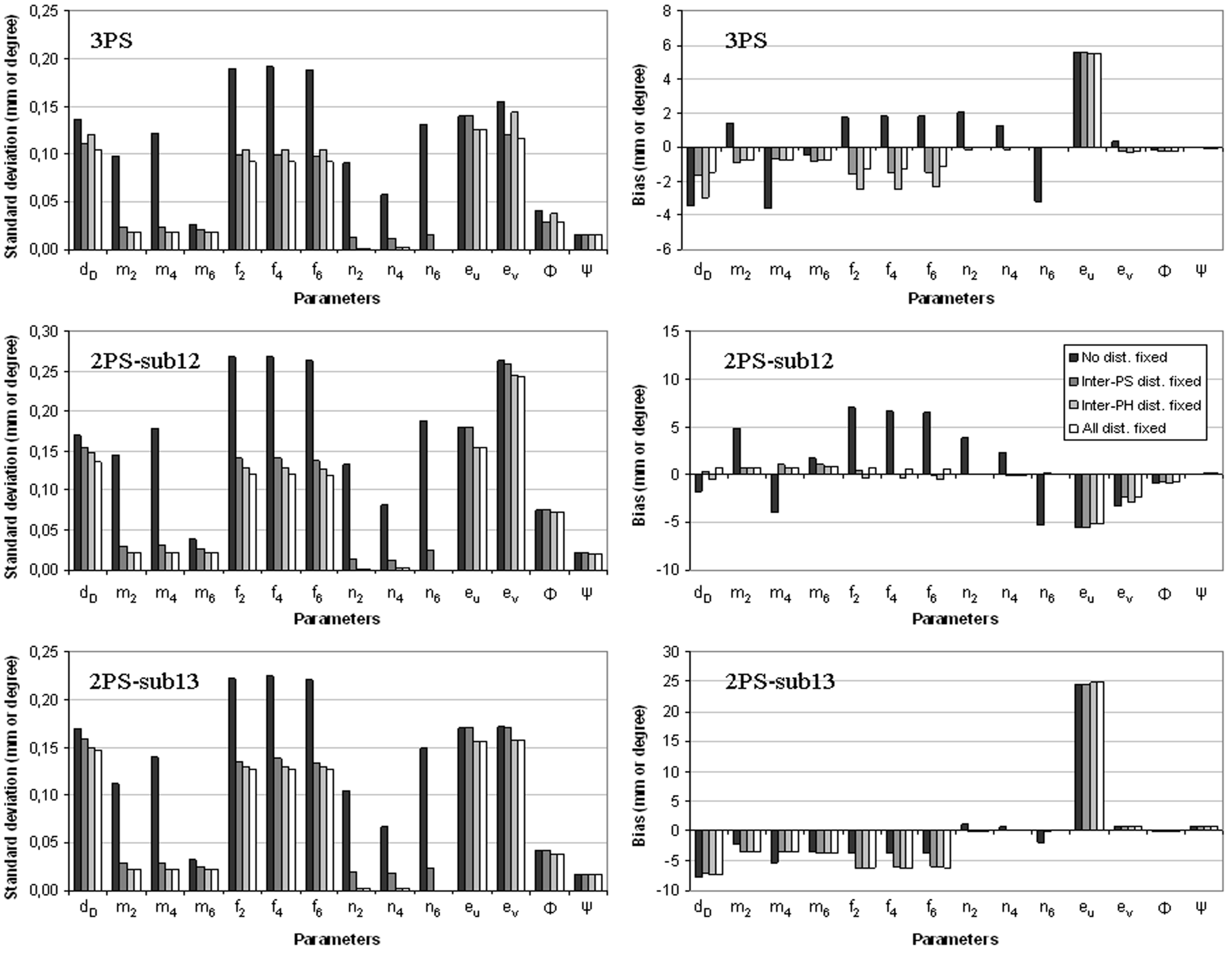

Fig. 4. Calibration accuracies with detector head 2, yielded with different calibration point settings and with truncated point projections. Top / middle / bottom row: 3PS / 2PS-sub12 / 2PS-sub13. Left / right column: standard deviation (ΔP_N) / bias (ΔP_B) on each parameter. Results of four calibration methods are plotted in cluster. The unit of error is either in mm or in degrees.

TABLE IV

RECONSTRUCTION ACCURACY IN CASE 1 (TRUNCATED PROJECTIONS)

	3PS		2PS-sub12		2PS-sub13	
Calibration with Head 1 Data	Res. Loss	Img. Def.	Res. Loss	Img. Def.	Res. Loss	Img. Def.
No distances fixed	0.024 (0.025)	0.761% (0.821%)	0.032 (0.031)	1.103% (1.108%)	0.039 (0.035)	0.859% (0.890%)
Inter-point distance(s) fixed	0.023 (0.025)	0.052% (0.058%)	0.029 (0.027)	0.132% (0.118%)	0.038 (0.033)	0.084% (0.083%)
Inter-pinhole distances fixed	0.012 (0.013)	0.055% (0.059%)	0.022 (0.021)	0.112% (0.105%)	0.016 (0.016)	0.057% (0.053%)
All distances fixed	0.011 (0.012)	0.041% (0.041%)	0.022 (0.022)	0.112% (0.112%)	0.016 (0.016)	0.056% (0.057%)
Calibration with Head 2 Data	Res. Loss	Img. Def.	Res. Loss	Img. Def.	Res. Loss	Img. Def.
No distances fixed	0.029 (0.028)	0.772% (0.822%)	0.034 (0.033)	1.129% (1.105%)	0.038 (0.035)	0.873% (0.920%)
Inter-point distance(s) fixed	0.026 (0.026)	0.054% (0.056%)	0.030 (0.033)	0.133% (0.122%)	0.037 (0.039)	0.086% (0.081%)
Inter-pinhole distances fixed	0.012 (0.013)	0.056% (0.061%)	0.022 (0.021)	0.113% (0.103%)	0.016 (0.016)	0.058% (0.057%)
All distances fixed	0.012 (0.012)	0.042% (0.042%)	0.022 (0.023)	0.113% (0.112%)	0.016 (0.016)	0.057% (0.055%)

Fig. 6 shows some maximum intensity projections of the reconstructions with calibration settings 2PS-sub12 and 2PS-sub13, reconstructed using the data of head 2 with refined calibration. It can be seen that the image deformation in the axial direction is very similar to that in the trans-axial direction (Fig. 5). The axial resolution is however difficult to compare since the phantom has little variation along the axis of rotation.

VI. DISCUSSION

In this study, we considered two sources of error in multi-pinhole SPECT calibration: random measurement noise and systematic orbit deviations. For fast estimation, we analyzed the error sources individually using an analytical linear model. Two measures, i.e., resolution loss and image deformation, are proposed as figures of merit to quantify the degradation of the image quality in the reconstruction image due to each of the disturbing factors. The theoretical results show that

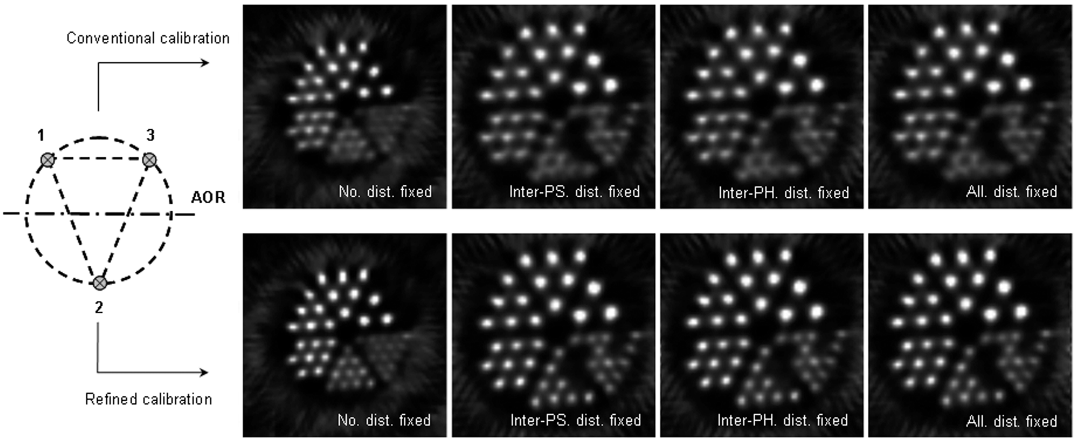

(a) Reconstructions with parameters estimated from the projection of 3 point sources (3PS)

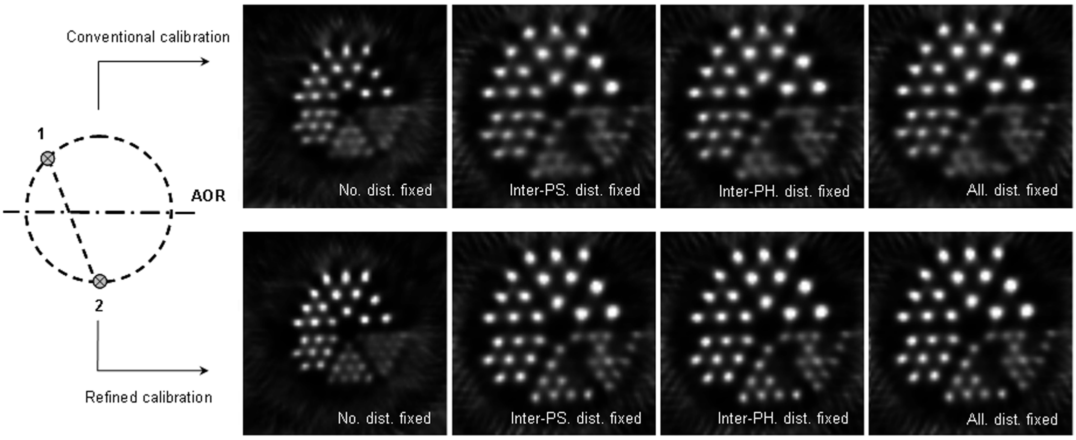

(b) Reconstructions with parameters estimated from the projection of 2 point sources (2PS-sub12)

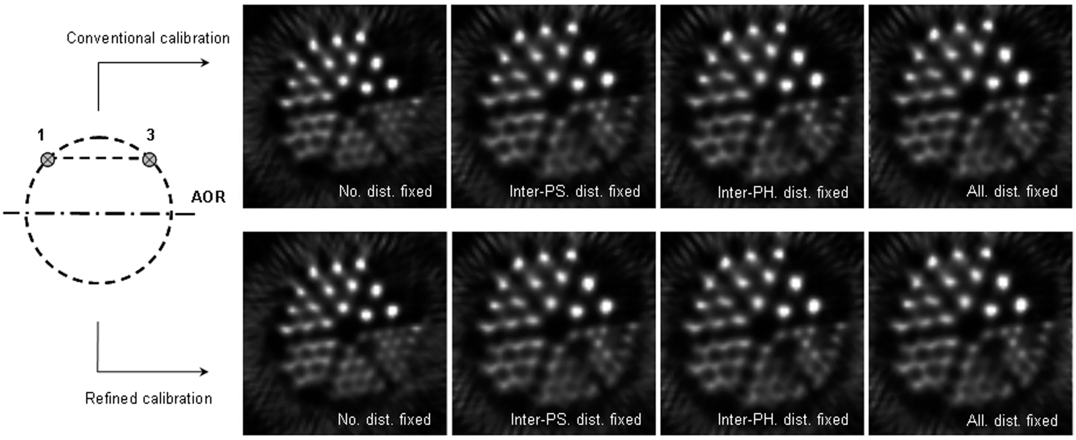

(c) Reconstructions with parameters estimated from the projection of 2 point sources (2PS-sub13)

Fig. 5. Trans-axial slices of Jaszczak phantom reconstructions, using the data from detector head 2. Top / middle / bottom group: with 3PS / 2PS-sub12 / 2PS-sub13 calibration setting. Upper / lower row in each group: reconstruction image with conventional / refined calibration. Left to right in each group: with four different calibration methods (No distance fixed, inter-point distance(s) fixed, inter-pinhole distances fixed and all distances fixed).

TABLE V
RECONSTRUCTION ACCURACY IN CASE 2 (TRUNCATED PROJECTIONS)

	3PS		2PS-sub12		2PS-sub13	
Calibration with Head 1 Data	Res. Loss	Img. Def.	Res. Loss	Img. Def.	Res. Loss	Img. Def.
No distances fixed	1.19 (1.10)	-28.8% (-30.8%)	1.00 (1.12)	-41.1% (-42.1%)	1.70 (1.42)	-22.0% (-22.3%)
Inter-point distance(s) fixed	1.42 (1.41)	1.83% (1.90%)	1.29 (1.33)	2.03% (2.11%)	1.90 (1.92)	-1.71% (-1.76%)
Inter-pinhole distances fixed	1.50 (1.48)	-1.01% (-0.93%)	1.18 (1.21)	1.16% (1.28%)	2.08 (2.09)	-1.81% (-1.90%)
All distances fixed	1.41 (1.40)	1.32% (1.40%)	1.29 (1.33)	1.62% (1.72%)	2.08 (2.09)	-1.82% (-1.90%)
Calibration with Head 2 Data	Res. Loss	Img. Def.	Res. Loss	Img. Def.	Res. Loss	Img. Def.
No distances fixed	2.38 (2.18)	-19.2% (-17.8%)	1.88 (1.89)	-31.0% (-28.6%)	3.02 (2.84)	-14.4% (-14.2%)
Inter-point distance(s) fixed	2.42 (2.36)	2.91% (2.79%)	2.20 (2.10)	3.54% (3.35%)	3.18 (3.22)	-4.03% (-4.44%)
Inter-pinhole distances fixed	2.00 (2.04)	-2.73% (-2.91%)	1.70 (1.67)	2.21% (-2.29%)	3.29 (3.30)	-4.13% (-4.56%)
All distances fixed	1.93 (1.94)	-2.14% (-2.22%)	1.80 (1.70)	2.73% (2.52%)	3.29 (3.30)	-4.13% (-4.56%)

TABLE VI
RECONSTRUCTION ACCURACY IN CASE 3 (TRUNCATED PROJECTIONS)

	3PS		2PS-sub12		2PS-sub13	
Calibration with Head 1 Data	Res. Loss	Img. Def.	Res. Loss	Img. Def.	Res. Loss	Img. Def.
No distances fixed	0.63 (0.66)	-28.7% (-30.8%)	0.54 (0.60)	-40.8% (-41.9%)	1.10 (1.26)	-21.8% (-22.4%)
Inter-point distance(s) fixed	0.44 (0.55)	0.87% (0.96%)	0.26 (0.40)	1.02% (1.12%)	0.95 (1.48)	-1.03% (-1.90%)
Inter-pinhole distances fixed	0.35 (0.49)	-0.34% (-0.44%)	0.26 (0.47)	0.25% (0.30%)	0.95 (1.47)	-1.11% (-2.04%)
All distances fixed	0.37 (0.47)	0.32% (0.42%)	0.25 (0.43)	0.62% (0.68%)	0.95 (1.47)	-1.11% (-2.04%)
Calibration with Head 2 Data	Res. Loss	Img. Def.	Res. Loss	Img. Def.	Res. Loss	Img. Def.
No distances fixed	1.02 (1.17)	-18.2% (-16.5%)	0.96 (0.87)	-30.5% (-28.1%)	1.95 (2.46)	-13.2% (-14.2%)
Inter-point distance(s) fixed	0.88 (1.14)	1.09% (1.43%)	0.71 (0.91)	1.24% (1.47%)	1.97 (2.78)	-2.47% (-4.38%)
Inter-pinhole distances fixed	0.62 (0.81)	-1.06% (-1.32%)	0.54 (0.58)	-0.62% (-0.61%)	1.93 (2.83)	-2.57% (-4.50%)
All distances fixed	0.52 (0.69)	-0.44% (-0.59%)	0.49 (0.54)	0.35% (0.40%)	1.93 (2.83)	-2.57% (-4.50%)

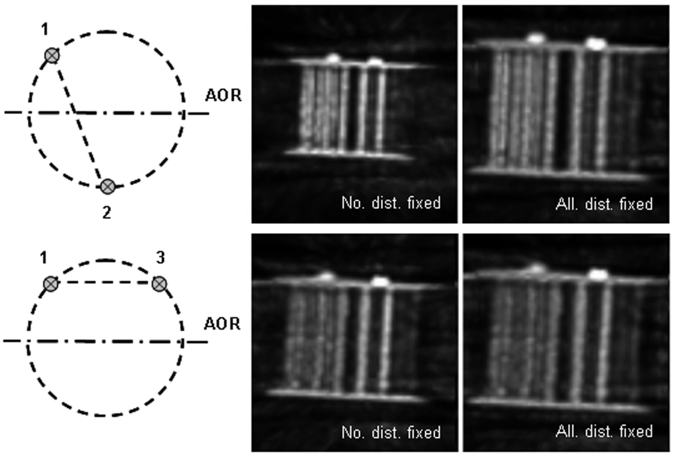

Fig. 6. Maximum intensity projections of Jaszczak phantom reconstructions. Top / bottom: with 2PS-sub12 / 2PS-sub13 calibration setting, using the data from detector head 2. Parameters were estimated by refined calibration.

the presence of systematic deviations plays a key role in the degradation of the reconstruction quality, whereas the data noise has a hardly observable effect on the accuracies of the reconstructed images.

In Fig. 4, not all the camera-specific parameters are given due to the limited space in the figure. For the pinhole locations, we only plot the results corresponding to the 2nd, 4th and 6th pinhole aperture. Actually, the results of the 3rd, 5th and 7th pinhole are somehow similar to those of the 6th, 2nd and 4th pinhole since their configurations are approximately symmetrical. In addition, one should note that the offset of the first pinhole n_1 was not fitted during the calibration but calculated from $n_1 = m_1 \tan\Psi$ [3]. This was done to determine the location of the origin of the coordinate system along the axis of rotation [18].

In table IV and V, the reconstruction errors predicted by the analytical method are always in good agreement with those calculated from simulations. In table VI, the predictions almost everywhere underestimate the image degradation when compared to the numerical simulations. This may indicate that the refined calibration did not completely eliminate the angular dependence of the parameters, as assumed in (37) and (38).

The refined calibration was initialized with the result of the conventional calibration and produced similar deformation and better resolution in all distance-fixing cases. As suggested in the introduction, we think that the refined calibration does not find an exact solution, but rather a nearby local minimum, and therefore suffers from very similar bias on the mean values of the (angle dependent) geometrical parameters. Although the refinement improves the reconstruction quality, it does not eliminate the problems due to this bias.

For the analytical study, we used a standard deviation of 0.6 mm to model the Gaussian noise. This value is derived based on the calibration results of real measurements. If we ignore the bias on the parameters, it is valid to assume that the difference between the measured projection and the refined-calibrated projection is only due to the noise in the measurement. The standard deviation on the difference between the measured and the estimated refined projection coordinates was around 0.6 mm in both $u-$ and $v-$ directions. Taking the bias into consideration will yield more accurate estimated projections, leading to an even smaller standard deviation. Therefore 0.6 mm is probably a pessimistic estimate for the noise. Nevertheless, as shown in the results, the influence of data noise is already negligible compared to that of systematic deviations.

The bias on the estimated parameters is determined by the given systematic deviations. Both the shape and the amplitude of the deviations greatly influence the result. In reality, the real pattern of the deviations is always unknown and can only be approximately estimated from previous refined calibrations. For the analytical study we only present the results with one set of typical systematic deviations. In fact, with all the calibration scans we ever performed, we have in total 23 different sets of systematic deviations. We applied these deviations to 3PS and repeated the analysis for detector head 2. For each calibration method, the standard deviation of 23 resolution loss values is about 0.2 mm for both case 2 and case 3. It means that the motion of the gamma camera cannot be precisely reproduced every time, and that the variation in the camera motion between the animal scan and the calibration scan may introduce extra resolution loss in the reconstruction. Therefore, if possible, it is preferable to acquire the animal data and the calibration data within one single acquisition.

Our method is general and applicable to any multi-pinhole system based on a circularly rotating detector. Since orbit deviations are very camera-specific and greatly influence the image quality, representative deviations need to be used when applying the method to another system.

Based on both the analytical results and the phantom experiment, we found that if no distance information is applied, the reconstruction may be remarkably scaled, both trans-axially and axially, with respect to the original size due to the lack of information about the pinhole magnification. Therefore we strongly recommend to use either the inter-point or inter-pinhole distances as prior knowledge during calibration. For the point sources, there are two typical approaches to fix their distances. The first one is to drill small holes on a rigid plate and fill them with radioactivity. The disadvantage is that it usually restricts the shape of the phantom, which compromises its use during the animal scan. This was the case with our Bequé phantom, therefore a separate calibration scan is demanded. The second approach is to attach the point sources to, e.g., the animal bed as separate markers, where special procedures are required to guarantee accurately known fixed distances between them [19]. Individual markers make it possible to perform a simultaneous animal-calibration scan, but it requires extra effort to guarantee the accurate inter-point distances. By contrast, fixing the inter-pinhole distances is more straightforward. Typically multiple apertures are drilled or eroded with high precision in a single rigid plate [5], [8], [16] or cylinder [6], [20]. Once the distances are accurately determined, they will be known for every scan with the same pinhole collimator. Combining this calibration approach with the individual point source markers (distance information is then not required) facilitates us to do simultaneous animal-calibration data acquisitions.

To determine the inter-pinhole distances accurately, one could either trust the specifications provided by the manufacturer, or acquire a large number of calibration scans, e.g., using a calibration phantom with point sources at accurately known distances, and then derive the distances between the apertures by averaging over all calibrations. We tried both approaches. Based on the difference between the fitted projection and the measured projection, we conclude that the averaged values derived from repeated calibrations are more reliable than the values provided by the manufacturer.

To facilitate discrimination between point source and animal projections, the use of two isotopes with sufficiently different energies is recommended. DiFilippo et al. suggested the use of Gadolinium-153 (^{153}Gd), which emits among others gammas of 97 keV and 103 keV (no higher-energy emissions) [19]. These energies can easily be discriminated from the photopeak energies of the most commonly used SPECT isotopes ($^{99\mathrm{m}}$Tc: 140 keV, ^{123}I: 159 keV). Additional advantages of using two distinct isotopes are the lower dose required to discern the point sources and the fact that a long-living isotope can be chosen, e.g., ^{153}Gd with a half-life of 242 days, such that the point sources do not need to be refilled for every calibration scan.

Usually one would expect that using more point sources for the calibration should always produce better results. This is true if the projection data is only disturbed by random noise. Indeed, in table IV, 3PS always results in better reconstruction accuracy than 2PS-sub12 and 2PS-sub13. However, it is not the same with the systematic deviation. In table V and VI, 3PS outperforms 2PS-sub13, but has slightly worse resolution than 2PS-sub12. We assume that if one uses projection data suffering from systematic deviations to do conventional calibration assuming perfect camera motion, the projection data actually carries ”inaccurate” information. If the additional point source carries less accurate information than the other two, it might make the results slightly worse.

The same principle also applies when we compare the results with and without truncation modeling (the analytical results related to the non-truncated case are not shown in this paper). With noise in the data, the reconstruction errors with truncated projections are always inferior to those with non-truncated projections due to the increase of uncertainty. However, when the projection data are subject to systematic deviations, most of the time we have slightly better results with truncated projections.

In agreement with the analytical prediction, the reconstruction images show that 2PS-sub13 yields larger reconstruction errors than 2PS-sub12, indicating that the position of the point sources strongly influences the calibration result. Hence it is of great interest to optimize the location of the point sources in order to minimize both the variance and the bias on the calibration parameters. In a previous study where only data noise was considered [21], it was found that the distance between the point sources, measured along the axis of rotation, should be as large as possible. The current study adds that the point sources should not be put on a line parallel to the rotation axis. More studies about the optimization of the point source locations will follow.

A phantom only provides anecdotal evidence, and since this particular phantom has no variation in axial direction, it only verified the predictions in two of the three dimensions. Nevertheless, the good agreement between the analytical predictions and the observed reconstruction quality of the Jaszczak phantom is encouraging.

VII. CONCLUSION

In this study, we extended an analytical linear approximation model, which was previously used to evaluate the noise propagation property of single pinhole SPECT, to investigate also the influence of systematic orbit deviations on multi-pinhole calibration. We used this method to estimate the bias and variance on each geometrical parameter (calibration accuracy), as well as the resolution loss and image deformation in the reconstructed image (reconstruction accuracy). Results show that small deviations between the actual orbit and the assumed circular orbit of the camera motion may introduce non-negligible bias on the estimated parameters, and that the reconstruction errors are dominated by this bias rather than by noise on the estimated coordinates of the point source projections. It is also shown that if no prior knowledge about any distance is applied, the dimension of the reconstruction image may be considerably scaled due to biased parameters. The two presented distance-fixing methods, i.e., fixing the inter-point source or inter-pinhole aperture distances, yield similar, improved reconstruction accuracy, however the latter is preferable since it facilitates simultaneous animal-calibration data acquisition. In addition, the reconstruction errors can be significantly reduced by carefully positioning the calibrating point sources.

APPENDIX

Assume the $1\times K$ matrix ΔP is a sample from a distribution with zero mean and known covariance matrix Cov(P). We wish to compute the variance on the value $H^T\Delta P$, where H is a linear operator ($1 \times K$ matrix). Here we show how Var$(H^T\Delta P) = H^T\text{cov}(P)H$ can be computed as the sum of K independent contributions.

With the matrix decomposition described in [15], the covariance matrix of the parameters Cov(P) can be expressed as

$$\text{cov}(P) = \Gamma\Gamma^T \tag{A-1}$$

The noise components in $k-$th column can be extracted by $\Delta P_k = \Gamma e_k$, with e_k the $k-$th unit vector. The variation ΔP_k can be linked to the measure of the reconstruction error by the linear operator H. This measure is thus $H^T\Delta P_k$, with squared value

$$\begin{aligned}(H^T\Delta P_k)^2 &= H^T\Delta P_k\Delta P_k^T H \\ &= H^T\Gamma e_k e_k^T\Gamma^T H \qquad \text{(A-2)}\end{aligned}$$

Adding all contributions quadratically yields:

$$\begin{aligned}\sum_{k=1}^{K}(H^T\Delta P_k)^2 &= \sum_{k=1}^{K}(H^T\Gamma e_k e_k^T\Gamma^T H) \\ &= \sum_{k=1}^{K} H^T\Gamma(e_k e_k^T)\Gamma^T H \\ &= H^T\Gamma I\Gamma^T H \\ &= H^T\text{cov}(P)H \qquad \text{(A-3)}\end{aligned}$$

where I is the identity matrix.

REFERENCES

[1] C. Vanhove, A. Andreyev, M. Defrise, j. Nuyts, A. Bossuyt. "Resolution recovery in pinhole SPECT based on multi-ray projections: a phantom study". *Eur J Nucl Med Mol Imaging*. vol. 34(2), pp. 170-180, 2007.

[2] G. Bal, P.D. Acton. "Analytical derivation of the point spread function for pinhole collimators." *Phys Med Biol*, vol. 51, pp. 4923-4950, 2006.

[3] D. Bequé, J. Nuyts, G. Bormans, P. Suetens, and P. Dupont, "Characterization of pinhole SPECT acquisition geometry." *IEEE Trans. Med. Imag.*, vol. 22(5), pp. 599-612, 2003.

[4] S. R. Meikle, P. Kench, A. G. Weisenberger, R. Wojcik, M. F. Smith, S. Majewski, S. Eberl, R. R. Fulton, A. B. Rosenfel and M. J. Fulham, "A prototype coded aperture detector for small animal SPECT." *IEEE Trans. Nucl. Sci.*, 49(5), 2167-2171, 2002.

[5] N. U. Schramm, G. Ebel, U. Engeland, T. Schurrat, M. Béhé, and T. Behr, "High-resolution SPECT using multipinhole collimation." *IEEE Trans. Nucl. Sci.*, vol. 50(3), pp. 315-320, 2003.

[6] F. J. Beekman and B. Vastenhouw, "Design and simulation of a high-resolution stationary SPECT system for small animals." *Phys. Med. Biol.*, vol. 49(19), pp. 4579-4592, 2004.

[7] K. Vunckx, D. Bequé, M. Defrise and J. Nuyts, "Single and multipinhole collimator design evaluation method for small animal SPECT." *IEEE Trans. Med. Imag.*, 27(1), pp. 36-46, 2008.

[8] C. Vanhove, M. Defrise, T. Lahoutte and A. Bossuyt, "Three-pinhole collimator to improve axial spatial resolution and sensitivity in pinhole SPECT." *Eur. J. Nucl. Med. Mol. Imaging*, 35, pp. 407-415, 2008.

[9] F. P. DiFilippo, "Design and performance of a multi-pinhole collimation device for small animal imaging with clinical SPECT and SPECT-CT scanners." *Phys. Med. Biol.*, 53, pp. 4185-4201, 2008.

[10] Y. C. Wang and B. M. W. Tsui, "Pinhole SPECT with different data acquisition geometries: Usefulness of unified projection operators in homogeneous coordinates." *IEEE Trans. Med. Imag.*, vol. 26(3), pp. 298-308, 2007.

[11] K. Vunckx, M. Defrise, D. Bequé, C. Vanhove, A. Andreyev, and J. Nuyts, "Geometrical calibration and aperture configuration design in multi-pinhole SPECT." *IEEE Internat. Symp. on Biomed. Imag.*, pp. 1403-1406, 2008.

[12] S. D. Metzler and N. H. Patil, "Measuring the variation in radius of rotation as a function of gantry angle for ultra-high-resolution pinhole SPECT." *IEEE Trans. Nucl. Sci.*, vol. 52(5), pp. 1236-1242, 2005.

[13] M. Defrise C. Vanhove and J. Nuyts, "Perturbative refinement of the geometric calibration in pinhole SPECT." *IEEE Trans. Med. Imag.*, vol.27, pp. 204-214, 2008.

[14] J. Nuyts, K. Vunckx, M. Defrise and C. Vanhove, "Small animal imaging with multi-pinhole SPECT." *Methods*, 48(2), pp. 83-91, 2009.

[15] D. Bequé, J. Nuyts, P. Suetens, and G. Bormans, "Optimization of geometrical calibration in pinhole SPECT." *IEEE Trans. Med. Imag.*, vol. 24(2), pp. 180-190, 2005.

[16] K. Vunckx, J. Nuyts, B. Vanbilloen, M. De Saint-Hubert, D. Vanderghinste, D. Rattat, F. M. Mottaghy, and M. Defrise, "Optimized multipinhole design for mouse imaging." *IEEE Trans. Nucl. Sci.*, vol. 56(5), pp. 2696-2705, 2009.

[17] H. M. Hudson and R. S. Larkin, "Accelerated image reconstruction using ordered subsets of projection data." *IEEE Trans. Med. Imag.*, 13(4), pp. 601-609, 1994.

[18] S. D. Metzler, K. L. Greer and R. J. Jaszczak, "Determination of mechanical and electronic shifts for pinhole SPECT using a single point source." *IEEE Trans. Med. Imag.*, vol.24(3), pp. 361-370, 2005.

[19] F. P. DiFilippo, M. J. Riffe, K. M. Harsch, N. P. McCabe and W. D. Heston, "Detached multipinhole small animal SPECT device with real-time calibration." *IEEE Trans. Nucl. Sci.*, vol. 53(5), pp. 2605-2612, 2006.

[20] F. P. DiFilippo, "Geometric characterization of multi-axis multi-pinhole SPECT." *Med. Phys.*, 35(1), pp. 181-194, 2008.

[21] K. Vunckx, L. Zhou and J. Nuyts. "Noise propagation in multipinhole SPECT calibration." *IEEE Nuclear Science Symposium Conference Record*, pp. 3166-3172, 2009.